



Deposited via The University of Leeds.

White Rose Research Online URL for this paper:

<https://eprints.whiterose.ac.uk/id/eprint/208166/>

Version: Accepted Version

Article:

Ye, J., Liu, Y., Yang, Y. et al. (2023) Testing, analysis and design of wire and arc additively manufactured steel bolted connections. *Engineering Structures*, 296. 116939. ISSN: 0141-0296

<https://doi.org/10.1016/j.engstruct.2023.116939>

©2023, Elsevier. This manuscript version is made available under the CC-BY-NC-ND 4.0 license <http://creativecommons.org/licenses/by-nc-nd/4.0/>. This is an author produced version of an article published in *Engineering Structures*. Uploaded in accordance with the publisher's self-archiving policy.

Reuse

This article is distributed under the terms of the Creative Commons Attribution-NonCommercial-NoDerivs (CC BY-NC-ND) licence. This licence only allows you to download this work and share it with others as long as you credit the authors, but you can't change the article in any way or use it commercially. More information and the full terms of the licence here: <https://creativecommons.org/licenses/>

Takedown

If you consider content in White Rose Research Online to be in breach of UK law, please notify us by emailing eprints@whiterose.ac.uk including the URL of the record and the reason for the withdrawal request.

1 **Testing, analysis and design of wire and arc additively manufactured**
2 **steel bolted connections**

3 Jun Ye⁵, Yunyi Liu¹, Yuanzhang Yang¹, Zhen Wang³, Ou Zhao⁴, Yang Zhao¹

4 1. *College of Civil Engineering and Architecture, Zhejiang University, Hangzhou, 310058, China*

5 2. *Center for Balance Architecture, Zhejiang University, Hang Zhou, 310014, China*

6 3. *Department of Civil Engineering, Zhejiang University City College, Hangzhou, 310015, China*

7 4. *School of Civil and Environmental Engineering, Nanyang Technological University, Singapore*

8 5 *School of Civil Engineering, University of Leeds, Leeds, LS2 9JT, UK S*

9 **Abstract**

10 Capitalizing on Wire and Arc Additive Manufacturing (WAAM), 3D printed steel has shown
11 significant potential in manufacturing large-scale steel structural elements in the construction
12 industry. Due to the intrinsic difference in material properties, the mechanical performance of
13 WAAM steel connections requires further investigation. In this paper, a total number of 24
14 WAAM steel coupon specimens with three different print layer orientations and 36 WAAM
15 single-shear bolted connection specimens with one bolt of different design configurations were
16 fabricated, dimensionally measured with 3D scanning technique, and tested under monotonic
17 tension. The failure modes and ultimate capacities of the bolted connections were analysed,
18 focusing on the print layer orientations of the WAAM steel plates. The current codified design
19 provisions and design approaches proposed in the literature for steel structures were further
20 evaluated by comparing the failure modes and ultimate capacities of the bolted connection
21 specimens. This research shows that specimens with different print layer orientations present
22 anisotropy phenomena in the coupon tests and bolted connection tests with differences of up to
23 10% and 20%, respectively. The relatively accurate predictions of the ultimate capacity of the

24 WAAM steel bolted connection specimens following the current steel design standards are
25 significantly compromised by predicting the incorrect failure modes, which could be attributed
26 to the influence of anisotropic material properties of the WAAM steel plates and the failure
27 modes of tilt-bearing and the end-splitting not being considered in current design provisions.
28 This research conducted systematic experimental investigations focusing on the material
29 properties of WAAM steel and the structural behaviours of WAAM single-shear bolted
30 connections, which could potentially promote the application of WAAM technology in
31 construction industry.

32 **Keywords:** 3D printing; Wire arc additive manufacturing; Single-shear bolted connections;
33 Failure modes; Design approaches

34

35

36 **1. Introduction**

37 Additive manufacturing (AM), also known as 3D printing, has attracted attention from the
38 construction industry because of its advantages in structural efficiency, geometric freedom,
39 customization, and reduced material waste, along with high integration with digital structure
40 designs [1]. Metal AM techniques can be classified into three major categories: Powder Bed
41 Fusion (PBF), Directed Energy Deposition (DED), and Sheet Lamination [2]. Wire and arc
42 additive manufacturing (WAAM), belonging to one of the DED techniques, uses traditional
43 welding tools to form structural members with deposited welding materials [1, 3]. Compared
44 to traditional subtractive manufacturing methods and other AM techniques, WAAM shows
45 significant potential in the construction industry for its fast production speed, low equipment
46 cost, high material utilization, and high sustainability [4].

47 The WAAM technology has been successfully used for the construction of the 3D printed
48 footbridge [5, 6], as shown in Figure 1. The successful implementation of the 3D printed bridge
49 demonstrated the significant potential of metal 3D technology as an alternative construction
50 method in the building of infrastructures with complex shapes. Structurally efficient WAAM
51 components with elegant appeal and complex shapes can be generated using topology and
52 layout optimization [7, 8]. This also emphasizes the importance of investigations on the
53 fundamental behaviour of 3D printed materials and components for further application in the
54 construction industry. Several research works have been conducted to investigate the WAAM
55 steel material properties [9-16]. For the component level, the cross-sectional behaviours of
56 WAAM components were investigated, including Buchanan et al. [17] and Laghi et al. [18] on

57 circular hollow section stub columns, Kyvelou et al. [19] on square hollow section stub columns,
58 Huang et al. [20, 21] on columns with different hollow sections, and Guo et al. [22] on T-stub
59 connections. However, the research on WAAM steel for bolted connections is still limited.



61 Figure. 1. 3D printed bridges: (a) a MX3D metal 3D printed footbridge [5], and (b) a small 3D printed
62 footbridge in shell form [6].

63 Bolted connections have already been widely used in steel construction and are the potential
64 option to assemble large scale metal 3D printed structures. The structural behaviours of bolted
65 connections are affected by various factors, including the contact interaction between the bolts
66 and their surrounding holes, the elastic-plastic relationships of materials, and the effect of large
67 deformations in the connected plates [15, 23-25]. The potential failure modes for a single-shear
68 single-bolt connection mainly include shear-out, bearing, and net section failure (except for bolt
69 shear) [26]. The design ultimate capacity of a bolted connection corresponding to those failure
70 modes has been specified in the different standards of cold-formed steel design codes and
71 guidelines, including AS/NZS 4600 [27], AS 4100 [28], AISI S100 [29], AISC 360 [30], EN
72 1993-1-1 [31], EN 1993-1-3 [32], and EN 1993-1-8 [33].

73 Design approaches for the shear connections were also proposed by researchers around the
74 globe to achieve more efficient designs. Based on the existing standards, Teh et al. [34-38]

75 defined a shear lag coefficient and an active shear plane to predict the ultimate capacities of net
76 section and shear-out failure modes, respectively, which had already been referenced by AISI
77 S100 [29] and AS/NZS 4600 [27]. Salih et al. [39, 40] established finite element models for
78 stainless steel bolted connections and proposed the design equations of the ultimate capacities
79 of stainless steel bolted connections for thin steel plates. Kim et al. [41-43] found that bolt
80 connections with thin plates under single shear were prone to out-of-plane deformations, and
81 revised the design equations considering the curling effect. Two failure modes not mentioned
82 in the standards, end-splitting and tilt-bearing, were observed in the experiments. Lyu et al. [44,
83 45] considered the end-splitting failure as the transitional failure mode between shear-out and
84 net section failure and proposed a new equation to predict the ultimate capacities considering
85 end-splitting failure. Distinguished from curl-bearing and localised tearing failure, a new
86 formula was proposed by Teh and Uz [46] for the tilt-bearing failure of the bolted connections
87 with thinner plates.

88 However, most of the current research works focusing on bolted connections are based on steel
89 manufactured by conventional methods. Ding et al. [47] highlighted the uniqueness of cold-
90 formed steel design in which local sheet bending can influence connection strength, as opposed
91 to hot-rolled steel for which such effects are safely ignored. This means that bolted connections
92 fabricated with different materials could show different failure modes and ultimate load-
93 carrying capacities. Guo et al. [48] tested the ultimate load-carrying capacities and failure
94 modes of WAAM steel single-shear bolted connections in two different nominal thicknesses,
95 two different print layer orientations, and varying dimensions. They preliminarily analysed the

96 mechanical characteristics of WAAM steel single-shear bolted connections and the prediction
97 accuracy of different standards. However, more comprehensive analyses are required to be
98 conducted based on further research and experimental data.

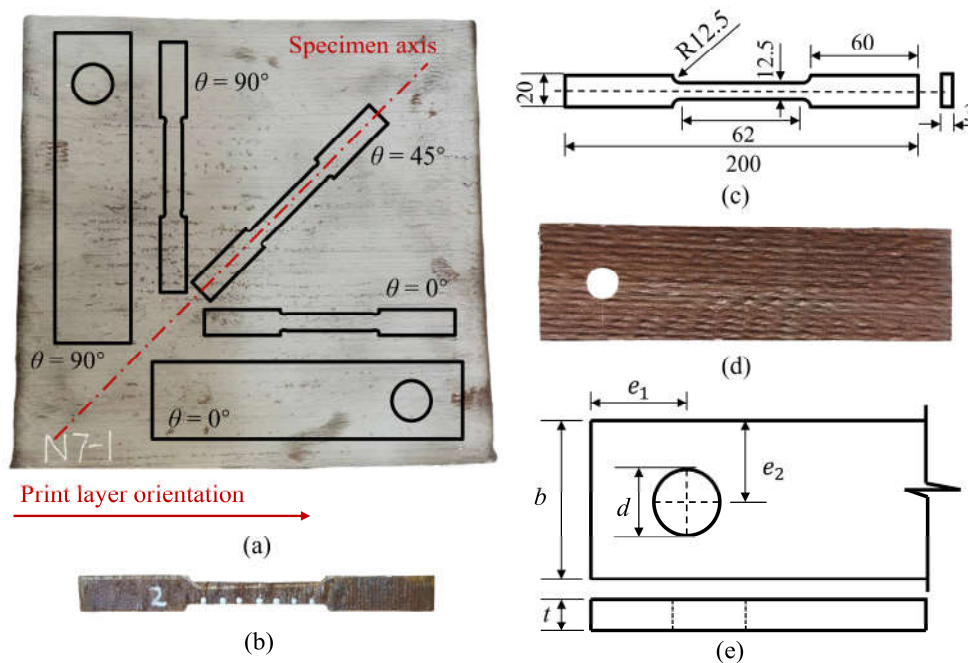
99 This paper presents an experimental programme regarding the mechanical properties and
100 structural behaviours of WAAM steel single-shear bolted connections subjected to monotonic
101 tension. A 3D laser scanner and a Matlab program are used to obtain the geometric properties
102 of WAAM steel specimens with undulating surfaces as the basis for discussion of WAAM steel
103 material properties. Twenty-four coupon specimens with three different print layer orientations
104 are tested under tension. A total number of 36 single-shear connection specimens with one bolt
105 with various plate dimensions, hole sizes, and hole positions were designed, fabricated from
106 WAAM plates, and tested with DIC measuring the displacement. The failure modes and
107 ultimate capacities of the bolted connections were analysed. The validity of the available
108 codified design provisions and design equations proposed in the current literature for
109 conventional thin-walled steel bolted connections were evaluated for the 3D printed steel plate
110 connections. This research conducted systematic experimental investigations focusing on the
111 WAAM steel specimens, which could potentially promote the application of WAAM
112 technology in construction industry.

113 **2. Experimental programme**

114 **2.1 Materials and specimens**

115 WAAM steel plates of 3 mm nominal thickness were extracted from the oval tubes with flat

116 sides manufactured using the WAAM process for the fabrication of the material and bolt
 117 connection specimens, as shown in Figure 2. The chemical compositions, mechanical properties,
 118 and printing parameters of ER50-6 low-carbon steel feedstock are listed in Table 1, Table 2,
 119 and Table 3, respectively. Although the manufacturing parameters, such as the heat input and
 120 the cooling rates, were not provided by the material supplier, the influence of the manufacturing
 121 parameters on the microstructure and material properties of the WAAM specimens could refer
 122 to the work of other researchers [10, 49].



123
 124 Figure 2. (a) Specimens extraction diagram from oval tubes with flat sides; (b) coupon with a θ of 90° ;
 125 (c) dimensions of the coupon; (d) bolted connection specimen with a θ of 0° ; and (e) dimensions of the
 126 bolted connection specimen.

127 Table 1. Chemical compositions (% by weight) of ER50-6 low carbon steel feedstock.

Chemical compositions	C	Mn	Si	P	S	Cr	Ni	Cu	Mo	V
ER50-6	0.074	1.47	0.85	0.015	0.01	0.023	0.009	0.1	0.004	0.002

128 Table 2. Mechanical properties of ER50-6 low carbon steel feedstock.

Tensile Strength (MPa)	Yield Strength (MPa)	Elongation Rate (%)	Charpy V Impact Test Value at 40°C (J)

ER50-6	554	445	26	96
--------	-----	-----	----	----

129 Table 3. Printing and environmental parameters of specimens with a nominal thickness of 3 mm.

Travel speed (m/min)	Wire feed rate (m/min)	Wire diameter (mm)	Welding voltage (V)	Layer thickness (mm)	Bead width (mm)	Temperature (°C)	Humidity (%RH)	Shielding gas
0.65-0.7	4.0	1.2	19.5	1.8	5	12-21	35-55	97%Ar+ 3%CO ₂

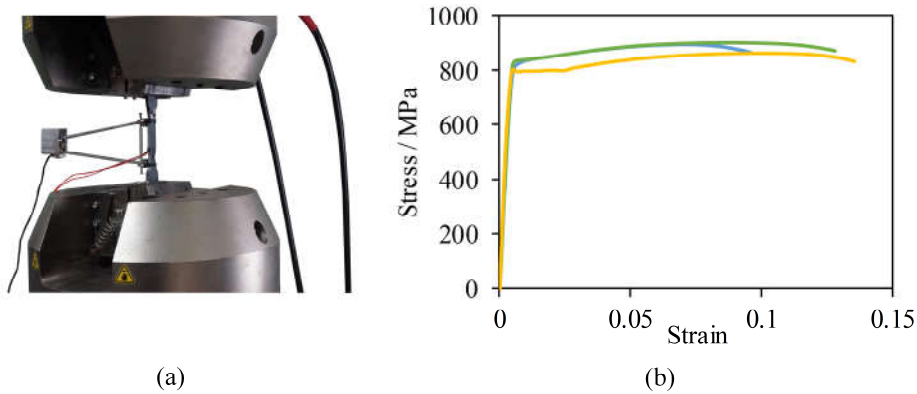
130 To investigate the effects of print layer orientations, tensile coupons were extracted from flat
 131 plates with three relative angles θ between the specimen axes and the print layer orientations
 132 of 0°, 45°, and 90°, as shown in Figure 2(a). In total, 24 tensile coupons (Figure 2(b)) with a
 133 nominal thickness of 3 mm were designed with the dimensions shown in Figure 2(c), including
 134 6 coupons with θ being 0°, 6 coupons with θ being 45°, and 12 coupons with θ being 90°.

135 The masses and volumes of the WAAM tensile coupons were obtained using an electronic scale
 136 and Archimedes' principle respectively. An average density value of 7692 kg/m³ was measured
 137 using masses dividing matched volumes. The obtained density was lower than 7850 kg/m³ of
 138 conventional low-carbon steel, which was in consistence with the experimental work conducted
 139 at Imperial College London [10]. The lower density could be attributed to the pores generated
 140 during the WAAM production process [49, 50].

141 Meanwhile, 36 WAAM steel bolted connection specimens of a nominal thickness of 3 mm were
 142 extracted from the oval tubes with two θ values (0° and 90°), as shown in Figure 2(a). Each
 143 specimen plate (Figure 2(d)) was named in the form of HS-*d-b-e*₁ or VS-*d-b-e*₁ with nominal
 144 dimensions, such as HS-18-30-27. The letter 'H' or 'V' means that the plate was extracted
 145 horizontally or vertically to the print layer orientation, with θ being 0° or 90°, respectively. The
 146 letter 'S' means the single-shear connection type. As shown in Figure 2(e), the nominal diameter

147 of the bolt hole and the nominal width of the bolted connection plate are represented by d and
 148 b , respectively. The letter e_1 is the minimum distance from the centre of the bolt hole to the
 149 end of the bolted connection plate.

150 High-strength Q690 steel plates with a nominal thickness of 4 mm were used to replace parts
 151 of WAAM steel plates in the bolted connections, to simplify the experimental variables and to
 152 ensure the failure occurring on the WAAM plates. Grade 12.9 high strength bolts and nuts were
 153 selected to prevent bolts from failing before the steel plates failed. The material properties of
 154 the high-strength Q690 steel plates were tested under the test setup shown in Figure 3(a) and
 155 the measured constitutive relationships are shown in Figure 3(b) and Table 4.



156

157

Figure 3. (a) Test setup, and (b) measured stress-strain curves for Q690 steel plates.

158

Table 4. Material properties of Q690 steel plates.

Specimens	Nominal thickness (mm)	Actual thickness (mm)	E (GPa)	f_y (MPa)	f_u (MPa)	ϵ_u	ϵ_f
1		4.3	237	819	896	0.07	0.10
2	4	4.2	217	835	901	0.09	0.13
3		4.2	199	803	862	0.10	0.16
Average	4	4.2	218	819	886	0.09	0.12

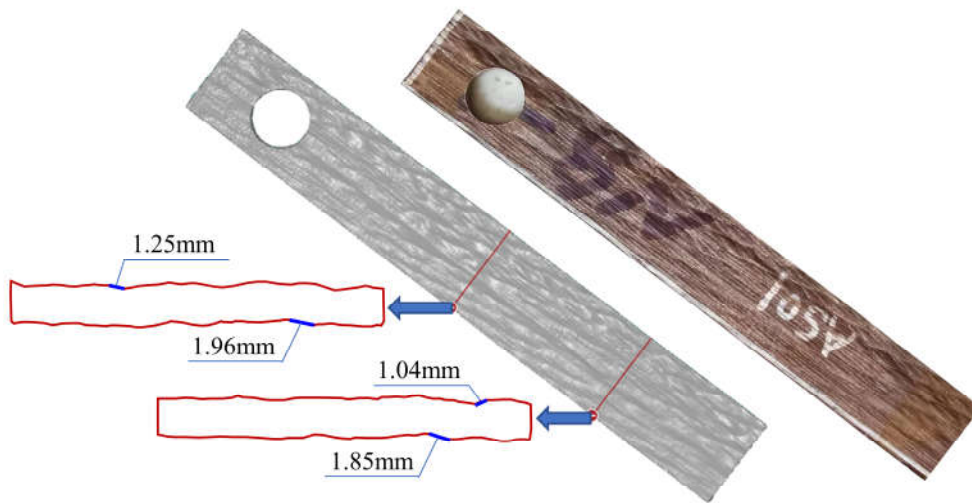
159

Note: E : Young's modulus; f_y : yield stress; f_u : ultimate tensile stress; ϵ_u : ultimate tensile strain, and ϵ_f : fracture strain.

160

161 **2.2 Geometric measurements**

162 All the WAAM steel specimens had undulating surfaces, as shown in Figures 2(b) and (d).
163 Therefore, it is almost impossible to measure the dimensions using traditional tools such as the
164 vernier calliper or micrometre calliper. To measure the geometric information of the specimens
165 in detail, a SIMSCAN 3D laser scanner was employed. The scanner can reach the maximum
166 scanning rate of 2020000 measurements per second, with an accuracy of 0.02 mm and a
167 maximum resolution of 0.025 mm. As shown in Figure 4, the selected laser scanner can
168 sufficiently capture the main geometric characteristics with the maximum resolution of 0.025
169 mm.

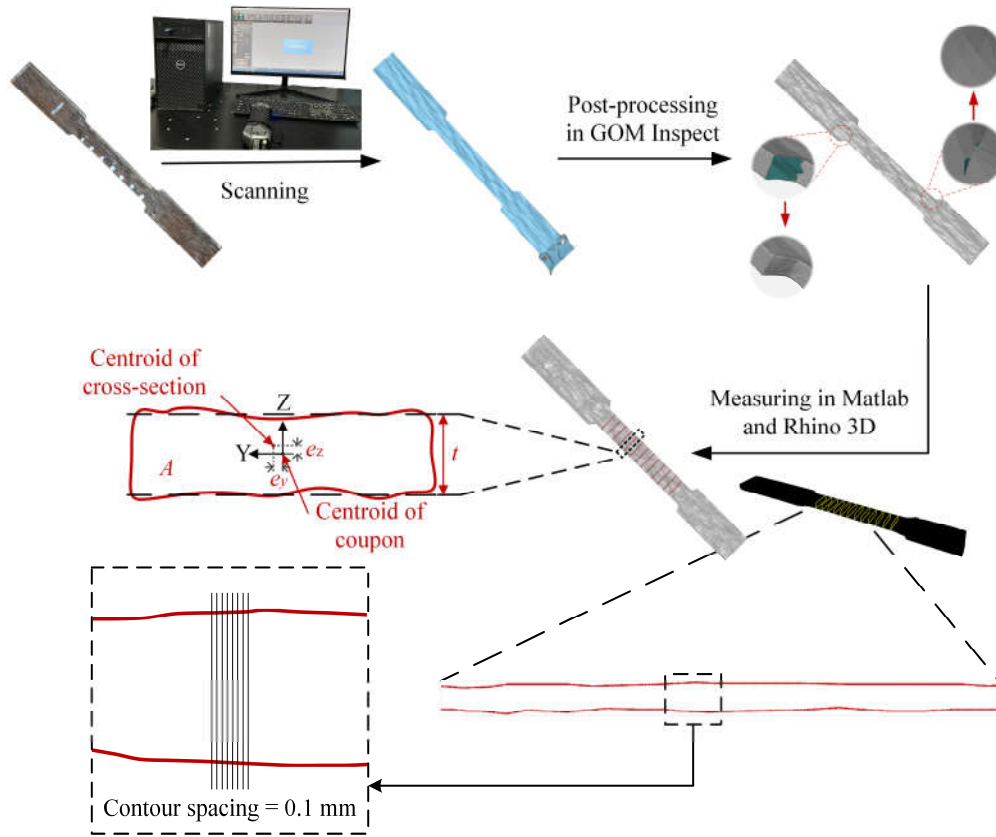


170

171 Figure 4. Surface undulation of the WAAM steel plates.

172 Figure 5 shows the whole scanning and measuring process. The test specimens were set up on
173 a flat table with calibration markers. The scan data was recorded in the form of point clouds
174 and imported into GOM Inspect for subsequent model post-processing such as eliminating grid

175 errors and repairing imperfections in the digital model. The volumes of the specimens can
176 therefore be measured via the digital models.



177

178

Figure 5. Scanning and measurement process of the WAAM plates.

179 To verify the accuracy of the scanner, the mass of each specimen was also recorded and its
180 corresponding actual volume was calculated using the measured density value of 7692 kg/m^3 .

181 The differences between the scanned volumes and measured volumes via the mass/density were
182 consistently within 2%, which verified the accuracy of the digital models.

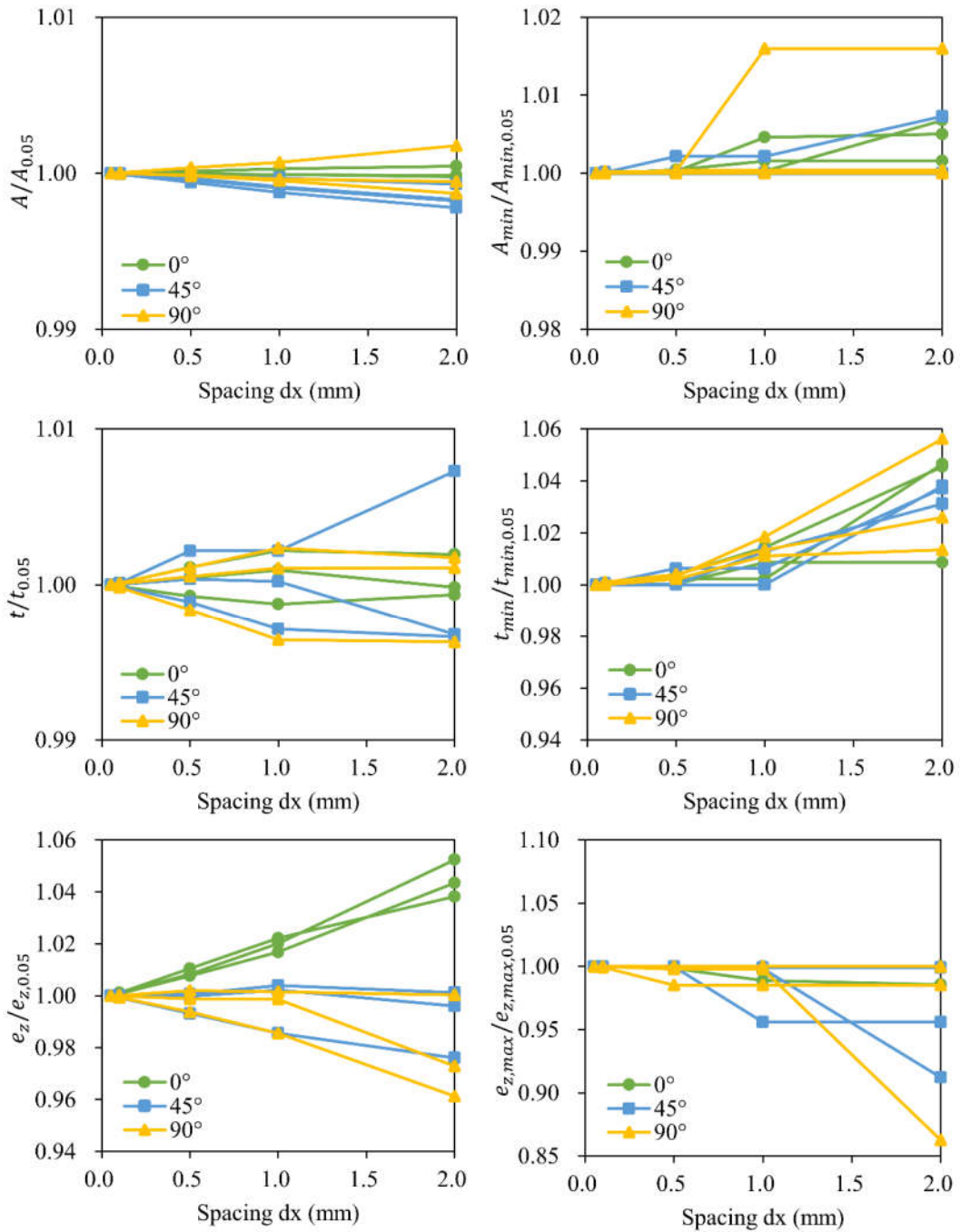
183 Further geometric measurements were conducted based on a Matlab program [10]
184 corresponding with Rhino 3D, which was developed by Imperial College London to calculate
185 the geometric properties of the WAAM steel specimens with inherent surface undulations. The

186 digital model without mesh errors and holes was first reoriented. The overall centroid of the
187 specimens coincided with the origin of the global coordinate system, with the plane of the
188 specimen paralleling to the XY plane, and the longitudinal axis of the specimens paralleling to
189 the X-axis. After the alignment operation, several closed polygons representing the rectangular
190 cross-sections were obtained by intersecting the specimen with planes in the same spacings
191 perpendicular to the X-axis.

192 A sensitivity study on the contour spacing was conducted, to accurately reflect the geometric
193 properties of the coupons while ensuring computational efficiency. Nine coupons were selected
194 for the sensitivity analysis (three for each print layer orientation), and the contour spacings were
195 set thinner than the typical WAAM bead widths [51] as 0.05 mm, 0.1 mm, 0.5 mm, 1 mm, and
196 2 mm.

197 The geometric properties calculated in various contour spacings were normalized according to
198 the results obtained with $dx = 0.05$ mm. Figure 6 shows the results of the sensitivity analysis
199 with various spacings, indicating that the average geometric properties (A , t , and e_z) were more
200 sensitive to the contour spaces than the extreme geometric properties (A_{\min} , t_{\min} , and $e_{z,\max}$). It
201 can be found that the geometric properties with a spacing of 0.1 mm were similar to that of 0.05
202 mm. Hence, $dx = 0.1$ mm was taken as the contour spacing value due to higher computational
203 efficiency.

204



205

206

Figure 6. Results of sensitivity study on different spacings.

207

For each coupon test specimen, the cross-section profiles were extracted from the parallel

208

segments of the specimens which were obtained from the process described above. Based on

209

the geometric measurement approach shown in Figure 5, the geometric results of the coupon

210 test specimens are shown in Table 5. The A_{std} and t_{std} values of the coupons with a θ of 0° were
 211 the minimum among three print layer orientation coupons, indicating the least variation in
 212 cross-sectional area and thickness along the X-axis. This is because all cross-sections
 213 perpendicular to the direction of the deposition paths are similar. In contrast, the dimensions of
 214 coupons with θ of 45° and 90° varied more in cross-sections. The average and maximum
 215 centroid eccentricities normalised by the corresponding average coupon thickness t , as well as
 216 their corresponding normalised standard deviations, increased with θ . Moreover, the
 217 eccentricities measured on the Y-axis were generally slightly higher than those on the Z-axis.

218 Table 5. Geometric properties of the WAAM coupons obtained from the analysis.

t_{nom} (mm)	θ ($^\circ$)	A (mm ²)	A_{min} (mm ²)	A_{std} (mm ²)	t (mm)	t_{std} (mm)	$\frac{ e_y }{t}$	$\frac{ e_{y,max} }{t}$	$\frac{ e_{y,std} }{t}$	$\frac{ e_z }{t}$	$\frac{ e_{z,max} }{t}$	$\frac{ e_{z,std} }{t}$
	0	42.3	40.8	0.80	3.4	0.25	0.03	0.07	0.02	0.01	0.04	0.01
3	45	44.3	39.7	3.09	3.6	0.42	0.05	0.15	0.04	0.04	0.12	0.03
	90	41.1	36.7	2.38	3.3	0.29	0.05	0.16	0.04	0.05	0.14	0.04

219 Note: t_{nom} represents the nominal thickness of the coupons; A , A_{min} , and A_{std} represent the average,
 220 minimum, and standard deviation values of the cross-sectional area along the X-axis; t and t_{std} represent
 221 the average and standard deviation values of thickness; e_y , $e_{y,max}$, and $e_{y,std}$ represent the average,
 222 maximum, and standard deviation values of the eccentricity between the centroid of coupon and cross-
 223 section along the Y-axis; e_z , $e_{z,max}$, and $e_{z,std}$ represent the average, maximum, and standard deviation
 224 values of the eccentricity along the Z-axis.

225 Meanwhile, for each bolted connection specimen, cross-section profiles were extracted from
 226 full-length specimens to represent its final measurement results. The obtained average
 227 measurements of the WAAM steel bolted connection specimens and high-strength Q690 steel
 228 bolted connection specimens are shown in Table 6 and Table 7, respectively. The high-strength
 229 Q690 steel bolted connection specimens were named following the same form of WAAM steel
 230 bolted connection specimens. ‘‘HSS’’ means high-strength steel. The Q690 HSS plates with

231 numbers “1” and “2” in Table 7 correspond to the WAAM steel plates with 0° and 90° print
 232 layer orientations, respectively. The minimum distance from the centre of a bolt hole to the edge
 233 of a bolted connection specimen was denoted as e_2 . The thickness t varied from 2.9 mm to 3.5
 234 mm, the width b varied from 30.2 mm to 69.8 mm, and the ratio of e_1 to e_2 varied from 0.5 to
 235 1.8. The diameter of the bolt hole was d while the nominal bolt diameter was denoted as d_f .

236

Table 6. Geometric measurement results of WAAM steel plates.

Specimens	t (mm)	d_f (mm)	d (mm)	b (mm)	e_1 (mm)	e_1/e_2
HS-18-30-27	3.1	16.0	17.8	30.3	26.6	1.8
HS-18-40-27	3.4	16.0	18.2	39.6	27.8	1.4
HS-18-60-20	3.0	16.0	18.0	60.4	21.8	0.7
HS-18-70-22	3.3	16.0	17.6	69.5	20.8	0.6
HS-18-60-18	3.4	16.0	17.8	60.3	15.4	0.5
HS-18-60-22	3.3	16.0	17.8	60.4	21.6	0.7
HS-18-60-32	3.1	16.0	18.0	59.9	30.2	1.0
HS-18-60-36	3.0	16.0	17.8	60.3	35.0	1.2
HS-18-70-36	3.4	16.0	18.0	69.6	37.2	1.1
HS-22-40-33	3.3	20.0	21.6	39.6	32.4	1.6
HS-22-50-33	3.5	20.0	21.6	50.8	31.0	1.2
HS-22-50-36	3.0	20.0	21.6	50.8	35.2	1.4
HS-22-60-26	3.1	20.0	21.6	60.3	27.4	0.9
HS-22-60-40	3.1	20.0	21.8	60.3	37.6	1.2
HS-26-50-39	3.4	24.0	26.2	50.9	39.4	1.5
HS-26-70-47	3.1	24.0	26.0	69.4	46.8	1.3
HS-26-60-29	2.9	24.0	26.2	60.6	27.8	0.9
HS-26-70-45	3.1	24.0	26.4	69.2	44.3	1.3
VS-18-30-27	3.3	16.0	18.0	30.2	26.4	1.7
VS-18-40-27	3.4	16.0	17.8	39.7	26.1	1.3
VS-18-50-20	3.1	16.0	17.6	50.7	19.8	0.8
VS-18-70-22	3.2	16.0	17.6	69.5	22.2	0.6
VS-18-60-18	3.2	16.0	18.0	60.2	17.8	0.6
VS-18-60-22	3.1	16.0	18.0	60.4	21.2	0.7
VS-18-60-32	3.5	16.0	17.8	60.2	30.7	1.0
VS-18-60-36	3.1	16.0	17.8	60.4	35.5	1.2
VS-18-70-36	3.3	16.0	18.0	69.9	35.2	1.0
VS-22-40-33	3.3	20.0	21.0	39.6	32.5	1.6

VS-22-50-33	3.1	20.0	21.6	49.8	32.2	1.3
VS-22-50-36	3.1	20.0	21.6	51.0	35.0	1.4
VS-22-60-26	3.2	20.0	21.6	60.3	24.6	0.8
VS-22-60-40	3.2	20.0	21.6	60.2	38.4	1.3
VS-26-50-39	3.1	24.0	21.6	49.7	38.6	1.6
VS-26-70-47	3.1	24.0	26.2	69.6	45.9	1.3
VS-26-60-29	3.2	24.0	26.4	60.5	27.6	0.9
VS-26-70-45	3.1	24.0	26.0	69.8	44.6	1.3

237

Table 7. Geometric measurement results of High-strength Q690 steel plates.

Specimens		t	d_f	d	b	e_1
		(mm)	(mm)	(mm)	(mm)	(mm)
HSS-18-30-27	1	4.0	16.0	18.0	31.2	26.1
	2	4.0	16.0	17.9	32.5	27.2
HSS-18-40-27	1	4.0	16.0	17.7	41.1	27.1
	2	4.0	16.0	17.5	41.4	24.7
HSS-18-60-20	1	4.0	16.0	17.5	61.4	19.3
	2	4.0	16.0	17.5	61.4	21.2
HSS-18-70-22	1	4.0	16.0	17.6	71.2	22.2
	2	4.0	16.0	17.7	71.6	22.3
HSS-18-60-18	1	4.0	16.0	17.5	60.7	17.8
	2	4.0	16.0	17.5	61.0	17.0
HSS-18-60-22	1	4.0	16.0	17.4	60.3	22.5
	2	4.0	16.0	17.4	61.5	22.4
HSS-18-60-32	1	4.0	16.0	18.1	61.3	33.0
	2	4.0	16.0	17.5	61.4	31.5
HSS-18-60-36	1	4.0	16.0	17.8	61.4	36.1
	2	4.0	16.0	17.3	60.9	35.3
HSS-18-70-36	1	4.0	16.0	17.9	71.4	35.8
	2	4.0	16.0	17.6	72.0	36.0
HSS-22-40-33	1	4.0	20.0	21.7	41.4	33.8
	2	4.0	20.0	21.9	40.9	33.3
HSS-22-50-33	1	4.0	20.0	22.1	51.3	32.9
	2	4.0	20.0	22.8	50.9	32.3
HSS-22-50-36	1	4.0	20.0	21.5	50.7	36.0
	2	4.0	20.0	21.9	51.7	36.5
HSS-22-60-26	1	4.0	20.0	22.6	61.3	26.8
	2	4.0	20.0	23.3	61.1	26.6
HSS-22-60-40	1	4.0	20.0	22.9	61.3	41.2
	2	4.0	20.0	23.4	61.5	40.4
HSS-26-50-39	1	4.0	24.0	25.9	51.0	38.5
	2	4.0	24.0	25.4	50.8	37.9

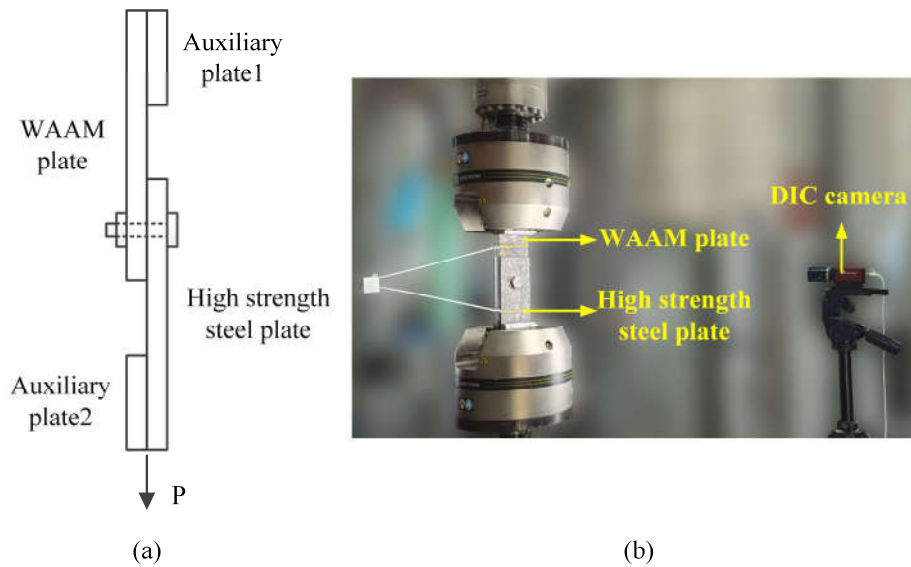
HSS-26-70-47	1	4.0	24.0	25.9	70.6	46.6
	2	4.0	24.0	25.3	70.7	46.6
HSS-26-60-29	1	4.0	24.0	26.3	60.7	28.8
	2	4.0	24.0	25.8	61.3	29.1
HSS-26-70-45	1	4.0	24.0	25.9	71.0	45.3
	2	4.0	24.0	25.9	71.0	45.3

238 Note: the measured geometric dimensions were obtained using Vernier calliper and micrometre calliper.

239 **2.3 Test Arrangements**

240 A total of 24 coupon tests and 36 bolted connection tests were conducted using a 250 kN Instron
 241 8802 testing machine under displacement control mode until fracture. The tensile coupons were
 242 tested at a constant stroke rate of 0.8 mm/min while the bolted connection specimens were
 243 tested at a stroke rate of 1.0 mm/min at room temperatures (20–25 °C) referring to the test
 244 arrangements of other researchers [52-54]. The bolted connection tests were stopped after
 245 reaching the ultimate load [55]. The loading details could be referred to the test by Huang et al.
 246 [56].

247 The bolted connection specimen was composed of a WAAM steel plate and a matched high-
 248 strength steel plate, connected by a high-strength bolt. The bolted connection specimens were
 249 vertically clamped on the tensile machine, as shown in Figure 7(a). Auxiliary plates were added
 250 at the clamping end to load the bolted connection specimens under concentric load. The contact
 251 between the bolts and steel plates was at the threaded portion of the bolt shank. All bolt nuts
 252 were finger tightened.



253

254 Figure 7. Schematic diagram of the experimental setup: (a) bolted connection and (b) typical test
 255 arrangement for bolted connections.

256 Due to the difficulty of installing strain gauges on the undulating surfaces of the WAAM steel
 257 plates, a non-contact full-field measurement method based on the Digital Image Correlation
 258 (DIC) technique, was adopted to produce a more detailed response field compared with
 259 traditional measurement methods [57]. Figure 7(b) shows the typical bolted connection test
 260 arrangement in the Instron testing machine with a DIC-based device. The speckle pattern was
 261 generated by spraying the surface of specimens with white and black paints. Calibration
 262 markers were also attached to the surface of specimens for DIC calibration. To obtain accurate
 263 correlation analysis results, the specimens were installed in a straight and parallel direction to
 264 the camera sensor, and the camera was set vertically to the ground. The acquired images were
 265 recorded at a frequency of 5 Hz.

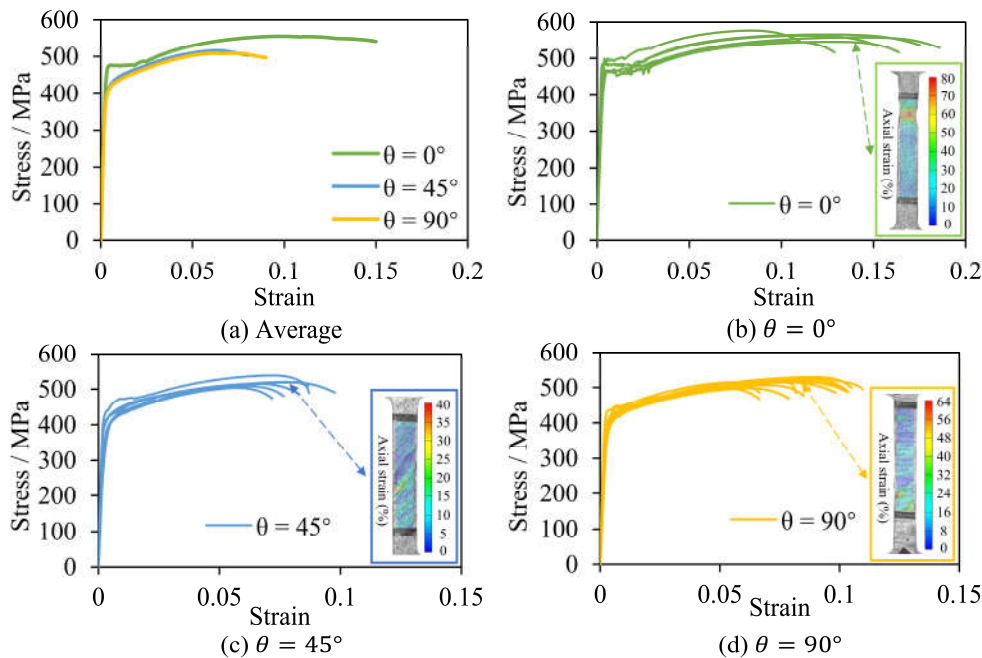
266 Both the conventional extensometer and DIC were set up to measure the displacement data,
 267 providing reliable verifications between each other. The conventional extensometer was fixed
 268 to the specimen and clamped with rubber bands. Specifically, the extensometer with a gauge

269 length of 50 mm was utilized for the coupons. For the bolted connection tests, a larger
 270 extensometer with a gauge length of 150 mm was employed to measure the displacement
 271 between the two connection lap plates.

272 3. Test Results

273 3.1 Observations for tensile coupon tests

274 The material properties of the coupons were calculated based on the average cross-sectional
 275 area (Table 5), with a subscript of "effective" added to the symbols, such as E_{eff} . The average
 276 and the stress-strain curves of all WAAM tensile coupons with θ of 0° , 45° , and 90° are shown
 277 in Figure 8. The average effective material properties, Young's modulus E_{eff} , yield stress $f_{y,eff}$,
 278 ultimate tensile stress $f_{u,eff}$, ultimate tensile strain $\varepsilon_{u,eff}$, and fracture strain $\varepsilon_{f,eff}$, derived from
 279 stress-strain curves are shown in Table 8.



280
 281 Figure 8. (a) Average stress-strain curves, and all stress-strain curves of WAAM tensile coupons with a

282

 θ of (b) 0° , (c) 45° , and (d) 90° .

283

Table 8. Average material properties for WAAM tensile coupons.

t_{nom} (mm)	t (mm)	θ ($^\circ$)	E_{eff} (GPa)	$\frac{E_{\text{eff}}}{E_{\text{eff},0^\circ}}$	$f_{y,\text{eff}}$ (MPa)	$\frac{f_{y,\text{eff}}}{f_{y,\text{eff},0^\circ}}$	$f_{u,\text{eff}}$ (MPa)	$\frac{f_{u,\text{eff}}}{f_{u,\text{eff},0^\circ}}$	$\varepsilon_{u,\text{eff}}$	$\frac{\varepsilon_{u,\text{eff}}}{\varepsilon_{u,\text{eff},0^\circ}}$	$\varepsilon_{f,\text{eff}}$	$\frac{\varepsilon_{f,\text{eff}}}{\varepsilon_{f,\text{eff},0^\circ}}$
	3.4	0	189	1.00	476	1.00	559	1.00	0.11	1.00	0.15	1.00
3	3.6	45	214	1.13	412	0.87	518	0.93	0.07	0.64	0.08	0.53
	3.3	90	198	1.05	408	0.86	515	0.92	0.07	0.64	0.09	0.60

284

Note: $E_{\text{eff},0^\circ}$, $f_{y,\text{eff},0^\circ}$, $f_{u,\text{eff},0^\circ}$, $\varepsilon_{u,\text{eff},0^\circ}$, and $\varepsilon_{f,\text{eff},0^\circ}$ is the average effective Young's modulus, yield stress, ultimate tensile stress, ultimate tensile strain, and fracture strain of WAAM tensile coupons with a θ of 0° .

285

286

287

Figures 8(b), (c), and (d) show the typical fractured coupons with different print layer orientations, along with the axial strain distributions visualised by the DIC system at the point of fracture. It was observed that the strain fields clearly reflected the starting point of the fractures and the print layer orientation of the coupons. Due to the undulating shapes, the coupons exhibited non-uniform strain fields with significant numerical fluctuations, but their average strains were consistent with the strains reflected by the extensometer within the gauge length.

288

289

290

291

292

293

294

From the stress-strain curves in Figure 8, it is shown that coupons with a θ of 0° had a clear yielding point. However, the other coupons did not have an explicit yielding phase. As a result, the yield stress was taken as the 0.2% proof stress. Figure 8 and Table 8 show that Young's modulus fluctuated at around 200 GPa. The average Young's modulus of the three groups of specimens with θ of 0° , 45° , and 90° were 189, 214, and 198 GPa, respectively, which could be influenced by the print layer orientations. Except for Young's modulus, the other material properties of specimens with a θ of 45° and 90° were consistently lower than those of

295

296

297

298

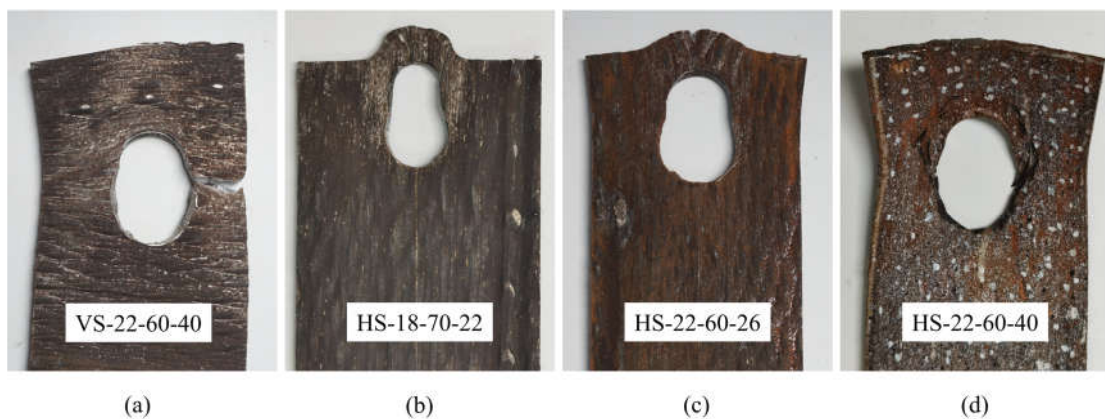
299

300

301 specimens with a θ of 0° , with differences of up to 13% and 14% for the yield stresses, 7%
302 and 8% for the ultimate stresses, 36% and 36% for the ultimate tensile strain, and 47% and 40%
303 for the fracture strain respectively, which showed anisotropic material properties of the WAAM
304 steel plates. Very limited difference in the material properties of specimens with θ of 45° and
305 90° was found and it was the reason for the print layer orientations selected for the bolted
306 connection tests with WAAM steel plates.

307 3.2 Observations from bolted connection tests

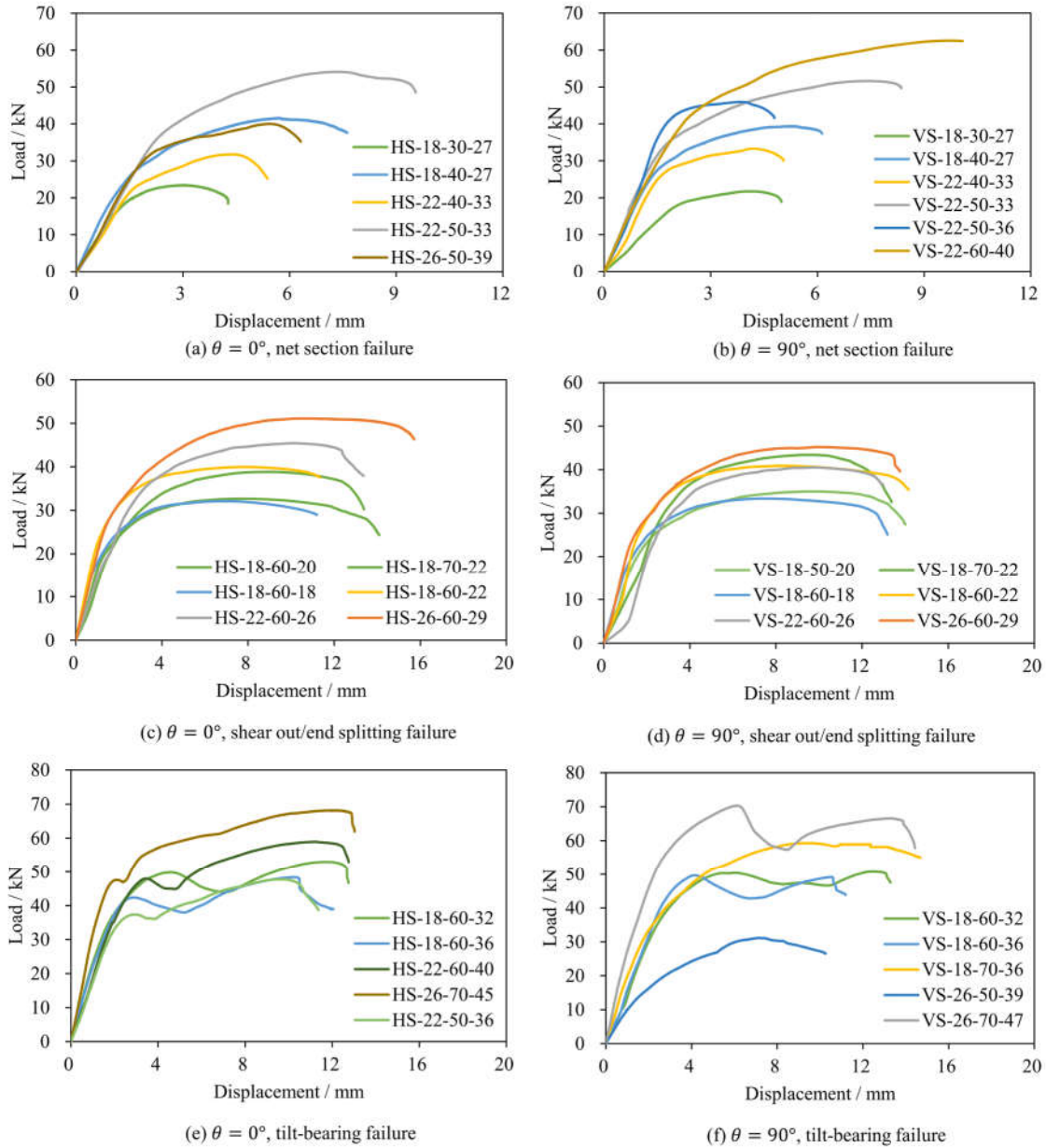
308 Four different failure modes, including net section, shear-out, end-splitting, and tilt-bearing
309 failure, were observed from the tests, as presented in Figure 9.



310 (a) (b) (c) (d)

311 Figure 9. Examples of failure modes: (a) net section, (b) shear-out, (c) end-splitting, and (d) tilt-bearing.
312 Net section failure developed in 12 bolted connection specimens with a small width (or net
313 width), considering that a small net section couldn't resist a large tensile action. It was observed
314 that an initial crack developed at the centre of the bolt hole, and a necking run across the net
315 section of the bolted connection plates, as shown in Figure 9(a). Figures 10(a) and (b) show
316 the load-displacement curves of specimens with net section failure for the bolted connections

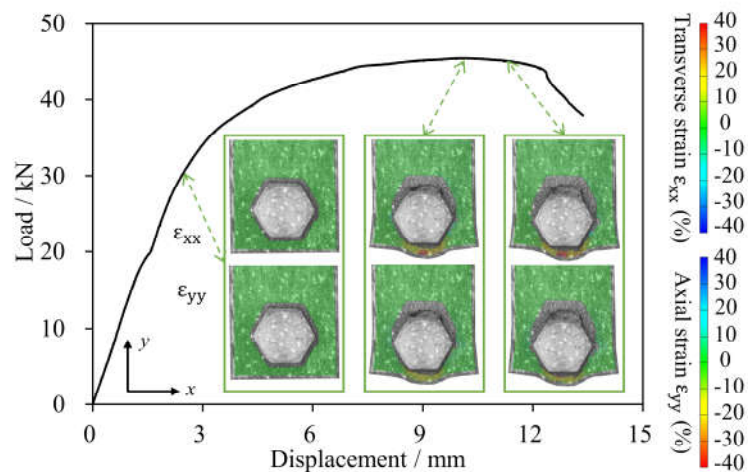
317 extracted from different print layer orientations. The load-displacement curves usually had one
 318 ultimate point, and the load declined after reaching the ultimate capacity.



319
 320 Figure 10. Load-displacement curve of WAAM steel bolted connection specimens failed at different
 321 failure modes.
 322 The bolted connection plates with small end distances e_1 cannot provide sufficient shear
 323 resistance with the limited shear planes, resulting in the shear-out failure for 10 bolted

324 connection specimens, as shown in Figure 9(b). It was also observed from Figures 10(c) and
325 (d) that every curve had an obvious platform. In the test process, it was observed that the
326 materials piled up in the front of the bolts until progressive fracture occurred and the materials
327 were pushed out.

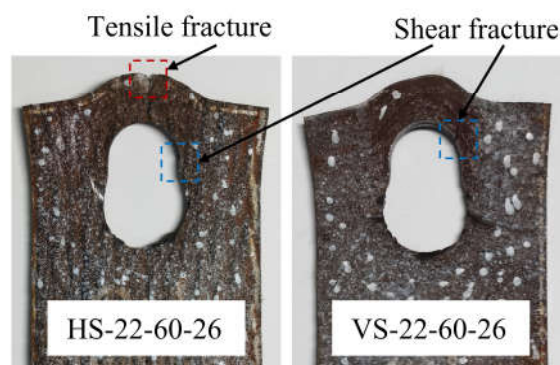
328 Only 3 specimens showed end-splitting failure in the tests, including HS-18-60-20, HS-22-60-
329 26, and VS-26-60-29. As shown in Figure 9(c), end-splitting failure is characterised by rotation
330 of net cross-section and transverse tensile fracture originating from the plate end. The axial
331 strain ϵ_{yy} fields and transverse strain ϵ_{xx} fields visualised by the DIC system for specimen HS-
332 22-60-26 are displayed in Figure 11. The colours of stress distributions were adjusted to make
333 it more convenient to compare the strains in two directions. It was observed that the high
334 transverse strain ϵ_{xx} was the controlling factor for end-splitting failure. The load-displacement
335 curves of specimens with end-splitting failure were incorporated into the shear-out failure
336 curves due to their similar failure behaviours, as shown in Figures 10(c) and (d).



337

338 Figure 11. Strain fields at different displacements for specimen HS-22-60-26.

339 Different from specimen VS-22-60-26, which failed by pure shear-out, specimen HS-22-60-26
340 exhibited a combination of shear-out and end-splitting failure. A similar failure mode was also
341 observed in the tests by Jiang et al. [58]. It presented both a tensile fracture at the tip of the
342 specimen and a shear fracture along the elongation area, as shown in Figure 12, which could be
343 attributed to high transverse strain ϵ_{xx} and axial strain ϵ_{yy} distributed in the specimen,
344 simultaneously.

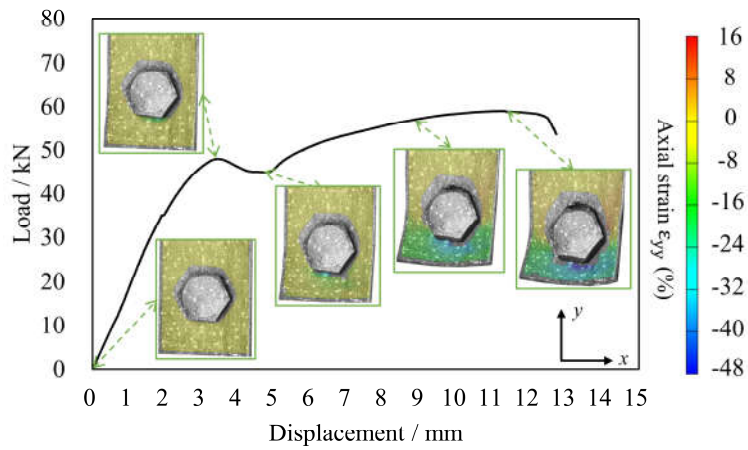


345

346 Figure 12. Comparison between specimens HS-22-60-26 and VS-22-60-26.

347 Tilt-bearing failure mode was observed in 12 specimens with the bolt head punching through
348 the upstream side of the bolt hole, bolt tilting, and plate curling, as shown in Figure 9(d). Figure
349 10(e) and (f) show the typical load-displacement curves of the bolted connections
350 corresponding to tilt-bearing failure mode. The curves usually had two peaks, and the first peak
351 was related to the curl of the plate. The axial strain ϵ_{yy} fields at different displacements obtained
352 by the DIC system for specimen HS-22-60-40 are displayed in Figure 13. The plate began to
353 curl after the first peak, and the axial tensile strain ϵ_{yy} in the downstream of the bolt hole
354 gradually increased as the stress was increased. Due to the presence of a bolt head, the strain
355 and fracture in the upstream of bolt hole cannot be clearly observed. Individual curves had only

356 one peak, even though the specimens still curled. Pure bearing failure was not discovered due
357 to the eccentricity of the applied load in the single shear connections.



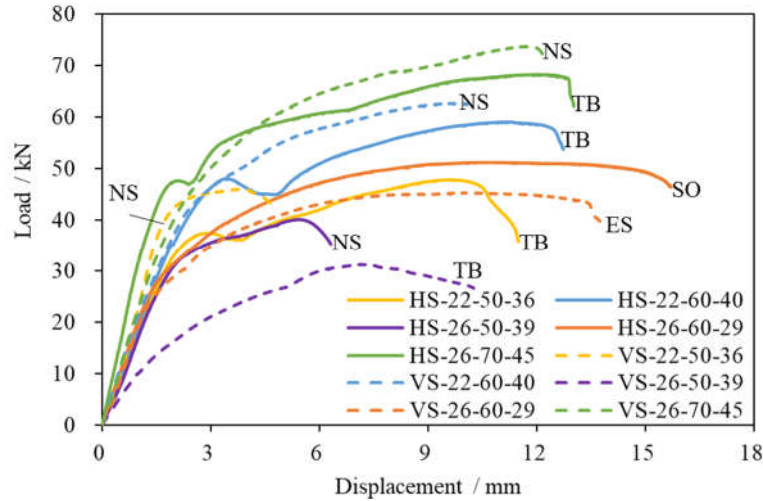
358

359 Figure 13. Strain fields at different displacements for specimen HS-22-60-40.

360 The print layer orientation had impacts on the responses of the bolted connection specimens,
361 including failure modes and ultimate capacities. Among all pairs of specimens with similar
362 dimensions but different print layer orientations, 29% of the pairs of specimens encountered
363 different failure modes. As shown in Figure 14, the 5 pairs of specimens showed different
364 failure modes in a total of 17 pairs of specimens, mainly including 4 pairs of different failures
365 of net section failure and tilt-bearing failure, and one pair of different failures of shear-out
366 failure and end-splitting failure. The VS specimens tended to present net section failure instead
367 of tilt-bearing failure, except for VS-26-50-39. However, they all followed the trend that the
368 specimens with net section failure had higher ultimate capacities and larger deformation than
369 those of specimens with tilting-bearing failure. HS-26-60-29 and VS-26-60-29 showed shear-
370 out failure and end-splitting failure respectively, and the former had a higher ultimate capacity

371 and larger deformation.

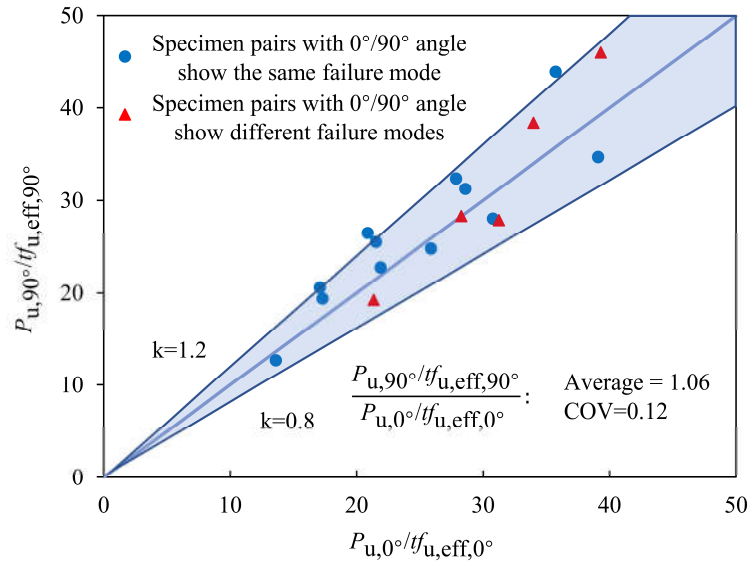
372



373

374 Figure 14. Load-displacement curves of the specimens with similar dimensions in different print layer
375 orientations resulting in different failure modes.

376 The normalised ultimate capacities $P_{u,0^\circ}/t_{u,eff,0^\circ}$ and $P_{u,90^\circ}/t_{u,eff,90^\circ}$ of the HS and VS WAAM steel
377 bolted connection specimens are compared in Figure 15. The ratios of $P_{u,90^\circ}/t_{u,eff,90^\circ}$ and
378 $P_{u,0^\circ}/t_{u,eff,0^\circ}$ were within the range from 0.8 to 1.2, indicating that the differences in the ultimate
379 capacity of the HS and VS specimens of the bolted connection tests were within 20%. This
380 showed that the ultimate capacities in the bolted connection tests were sensitive to the print
381 layer orientations. The red triangles in Figure 15 represent the five pairs of specimens with
382 different failure modes mentioned in the previous section. The triangles were distributed
383 differently without special rules, which could be attributed to the limited specimens being tested
384 and further experimental investigations are required in the future.



385

386 Figure 15. Comparison of different print layer orientations on ultimate capacities of bolted connection
 387 tests.

388 4. Design codes

389 The development of accurate and reliable design stipulations is important for the wider
 390 application of WAAM structures in the construction industry. In this section, the ultimate
 391 capacities of the tested specimens were evaluated against the predictions provided by the design
 392 rules stipulated in available design standards, namely AS/NZS 4600 [27], AS 4100 [28], AISI
 393 S100 [29], AISC 360 [30], EN 1993-1-1 [31], EN 1993-1-3 [32], and EN 1993-1-8 [33]. The
 394 proposed design rules from the recent literature were also evaluated with the test results to
 395 assess their suitability for the WAAM steel bolted connection design.

396 4.1 AS/NZS 4600 & AS 4100

397 4.1.1 AS/NZS 4600:2018 [27]

398 The ultimate capacities corresponding to different failure modes of a single bolt connection in

399 the cold-formed sheet are specified in AS/NZS 4600:2018 [27]. When bearing capacities are
 400 calculated without considering bolt hole deformation, the nominal tensile capacity $P_{ns,NZS}$ of the
 401 net section of the connection plate is:

$$P_{ns,NZS} = [0.9 + (\frac{0.1d_f}{b})]A_n f_u \quad (1)$$

402 where, d_f is the nominal bolt diameter; b is the width of the plate in the bolted connection; A_n
 403 is net sectional area of the connection plate; and f_u denotes the tensile strength of the connection
 404 plate.

405 The nominal shear-out capacity $P_{so,NZS}$ of the connection plate is:

$$P_{so,NZS} = e_1 t f_u \quad (2)$$

406 where, t is the thickness of the connection plates; and e_1 is the distance between the centre of a
 407 standard bolt hole to the end of the connection plate.

408 The nominal bearing capacity $P_{b,NZS}$ of the connection plate is:

$$P_{b,NZS} = \alpha C d_f t f_u \quad (3)$$

409 where, α = a modification factor, α is set as 0.75 for the single shear bolted connection without
 410 washers; C = bearing factor, when $d_f/t < 10$, $C = 3.0$; when $10 < d_f/t < 22$, $C = 4 - 0.1(d_f/t)$; and
 411 when $d_f/t > 22$, $C = 1.8$.

412 **4.1.2 AS 4100:2020 [28]**

413 The ultimate capacities of cold-formed steel bolted connections corresponding to various
 414 failure modes are specified in AS 4100:2020 [28]. When bearing capacities are calculated
 415 without considering bolt hole deformation, the nominal tensile capacity $P_{ns,AS}$ of the net section
 416 of the connection plate is:

$$P_{ns,AS} = 0.85A_n f_u \quad (4)$$

417 The nominal shear-out capacity $P_{so,NZS}$ of the connection plate is:

$$P_{so,AS} = (e_1 - \frac{d}{2})tf_u \quad (5)$$

418 where, d is the nominal bolt hole diameter.

419 The nominal bearing capacity $P_{b,NZS}$ of a bolted connection is:

$$P_{b,AS} = 3.2d_f tf_u \quad (6)$$

420 **4.2 AISI S100& AISC 360**

421 **4.2.1 AISI S100:2016 [29]**

422 The ultimate capacities of a bolted connection in the cold-formed sheet are specified in AISI
423 S100:2016 [29]. When the bearing capacities are calculated without considering bolt hole
424 deformation, the nominal tensile capacity $P_{ns,AISI}$ of the net section and the nominal bearing
425 capacity $P_{b,AISI}$ of the connection plate is the same as AS/NZS 4600:2018 [27], following
426 Equation (1) and (3). The nominal shear-out capacity $P_{so,AISI}$ of the connection plate is:

$$P_{so,AISI} = 1.2(e_1 - \frac{d}{2})tf_u \quad (7)$$

427 **4.2.2 AISC 360:2022 [30]**

428 The load-carrying capacities of a single bolt connection corresponding to various failure modes
429 in cold-formed sheets are also specified in AISC 360:2020 [30]. The nominal tensile capacity
430 $P_{ns,AISC}$ of the net section of a connection plate is:

$$P_{ns,AISC} = A_n f_u \quad (8)$$

431 The nominal shear-out capacity $P_{so,AISC}$ of the connection plate is:

$$P_{so,AISC} = 1.5(e_1 - \frac{d}{2})t f_u \quad (9)$$

432 The nominal bearing capacity $P_{b,AISC}$ of the connection plate is:

$$P_{b,AISC} = 3d_t t f_u \quad (10)$$

433 **4.3 Eurocode**

434 **4.3.1 EN 1993-1-1:2020 [31]**

435 The nominal tensile capacity $P_{ns,EN1}$ of the net section of a connection plate determined by EN
 436 1993-1-1:2020 [31], is shown in Equation (11), which is also incorporated into EN 1993-1-
 437 8:2021 [33] for connection design.

$$P_{ns,EN1} = k A_n f_u \quad (11)$$

438 where, $k = 1$, for plates with smooth holes fabricated by drilling or water jet cutting, or $k = 0.9$,
 439 for plates with rough holes fabricated by punching or flame cutting.

440 **4.3.2 EN 1993-1-3:2022 [32]**

441 According to EN 1993-1-3:2022 [32], the nominal tensile capacity $P_{ns,EN3}$ of the net section of
 442 the connection plate is:

$$P_{ns,EN3} = (1 + 3(\frac{d}{b} - 0.3)) A_n f_u \quad (12)$$

443 where, $(1 + 3(d/b - 0.3)) \leq 1$.

444 The nominal tensile capacity P_{EN3} of the shear out and bearing of the connection plate is

$$P_{EN3} = 2.5\alpha_b k_t d_t t f_u \quad (13)$$

445 where, α_b is the minimum value of 1 and $e_1/3d_t$; when $0.75 \text{ mm} < t < 1.25 \text{ mm}$, $k_t = (0.8t+1.5)/2.5$,
446 and when $t > 1.25 \text{ mm}$, $k_t = 1$.

447 **4.3.3 EN 1993-1-8:2021 [33]**

448 According to EN 1993-1-8:2021 [33], the nominal tensile capacity P_{EN8} of the shear out and
449 bearing of the connection plate is:

$$P_{EN8} = \alpha_b k_m d_t t f_u \quad (14)$$

450 where, α_b is the minimum of e_1/d , $3f_{ub}/f_u$, and 3; for steel grades equal to or higher than S460,
451 $k_m = 0.9$; otherwise $k_m = 1$.

452 **4.4 Design equations proposed in the literature**

453 Teh and Uz [37] modified Eq. (7) by proposing an active shear length, L_{av} , instead of a net shear
454 length, where $L_{av} = e_1 - d/4$.

$$P_{so} = 1.2(e_1 - \frac{d}{4})t f_u \quad (15)$$

455 A modification of Eq. (16) had been proposed by Xing et al. [35] considering the catenary
456 action which has a significant effect on the shear out capacity.

$$P_{so} = 1.2(\frac{3d_f}{e_1})^p (e_1 - \frac{d}{4})t f_u \quad (16)$$

457 where, p = the influence degree of catenary action, taken as 1/10 herein for the single-shear
458 single-bolt connections.

459 Lyu et al. [45] proposed a new Eq. (17) for the prediction of ultimate bearing capacity taking
460 into account splitting failure. The reduction factor ϕ varies in the value of e_1/d , but their

461 relationship shows a complicated feature. The reduction factor was recommended as $\varphi = 0.9$
462 [45].

$$P_{so} = \begin{cases} 1.04 \frac{e_1}{d} d_f t f_u, e_1/e_2 \leq 0.5 \\ \varphi P_{so}, e_1/e_2 > 0.5 \end{cases} \quad (17)$$

463 Equation (18) was also proposed for determining the ultimate tilt-bearing capacity [46], which
464 is distinguished from the conventional bearing failure.

$$P_{tb} = 2.65(b - d)d_f^{\frac{1}{2}}t^{\frac{4}{3}}f_u \quad (18)$$

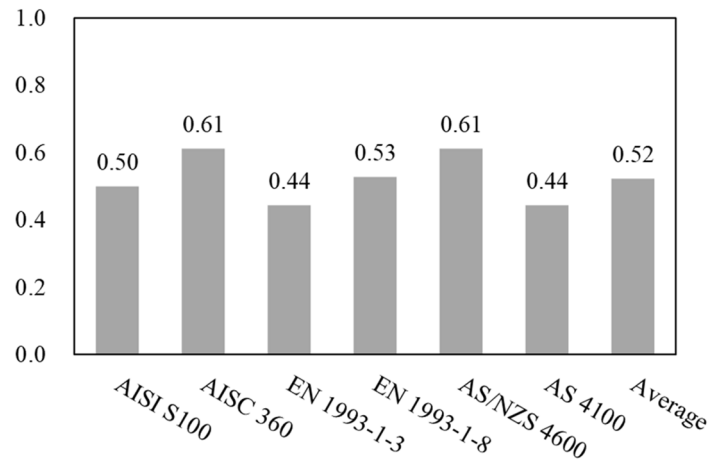
465 **5. Comparisons between test results and various design equations**

466 **5.1 Failure mode comparison results**

467 The standards were used to calculate the ultimate capacities related to different failure modes
468 including net section, shear-out, and bearing failures, according to the size information of the
469 specimens. The failure mode corresponding to the lowest ultimate capacity was considered as
470 the failure mode predicted by the standards. The experimental results of the failure mode were
471 compared with the predictions following the design approaches, as shown in Appendix A.

472 The overall prediction accuracies of the six standards for failure modes were not very satisfying.
473 The highest accuracy rate was acquired by AISC 360 [30] and AS/NZS 4600 [27], reaching
474 0.61, as shown in Figure 16. Part of the reason is that tilt-bearing and end-splitting failure are
475 not involved in the standards, which led to the wrong judgment of failure modes when the
476 experimental failure modes were tilt-bearing and end-splitting failure. It is suggested that the

477 future design codes or guidelines specialised for 3D printed steel structures should involve the
478 two failure modes that have not been specified in current design provisions.



479

480 Figure 16. Prediction accuracies of failure modes in six standards.

481 5.2 Ultimate capacities comparing with various design methods

482 The experimental results of ultimate tensile capacities were compared with the predictions
483 following the design approaches reviewed in Appendix A. In general, the design standards
484 presented showed different degrees of underestimation with the mean of test-to-predicted
485 capacity ratio P_{exp}/P_{pre} varying from 1.03 to 1.48.

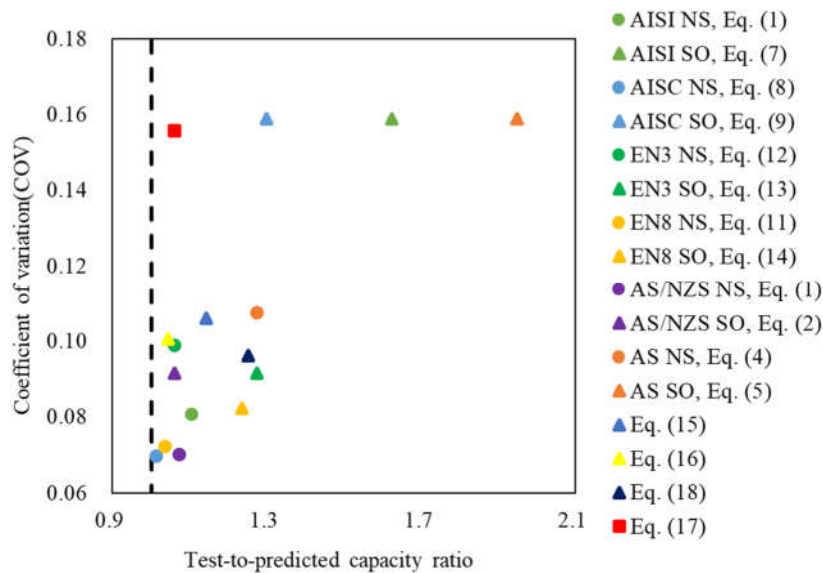
486 AS/NZS 4600 [27] performed the best in the six standards with both the lowest average test-
487 to-predicted capacity ratio of 1.03 and a coefficient of variation (COV) of 0.11. The
488 underestimation of the ultimate capacity of the connections was only 3%. Whilst, AS 4100 [28]
489 was the least accurate and stable with the highest underestimation of the ultimate load-carrying
490 capacity by 32% with a COV of 0.27.

491 To evaluate the applicability of the existing design approaches on WAAM steel bolted

492 connections, further analysis will be conducted in the following sections corresponding to
 493 different failure modes. The prediction accuracy of the design approaches proposed in the
 494 current literature for a particular failure mode will be discussed in Sections 5.3-5.6.

495 5.3 Net section failure

496 Figure 17 presents the test-to-predicted capacity ratio and the coefficient of variation for various
 497 design codes of practice. When the failure mode of the WAAM steel plate was net section
 498 failure, the test-to-predicted capacity ratio predicted by each specification fluctuated between
 499 1.01 and 1.27, and the COV lay between 0.07 and 0.11. The average predicted ultimate capacity
 500 of net section failure in AISC 360 [30] was the most accurate, reaching an average ratio of 1.00,
 501 with a COV of less than 0.07. The predictions of ultimate capacities for specimens with net
 502 section failure were generally accurate and stable, except for AS 4100 [28].



503

504

Figure 17. Evaluation of different codes towards different failure modes.

505 **5.4 Shear-out failure**

506 When the failure mode of the WAAM steel plate was a shear-out failure, the average test-to-
507 predicted capacity ratio and COV changed significantly for various design standards. This was
508 due to the different shear planes and shear coefficients used in the equations for shear-out failure.
509 Among all the design standards, AS/NZS 4600 [27] and Equation (16) performed the best with
510 an underestimation of 6% and 4%, with a COV of 0.09 and 0.10, respectively. The test-to-
511 predicted capacity ratios of AISC 360 [30], AISI S100 [29], and AS 4100 [28] were larger than
512 1.30 and the test-to-predicted ratios were scattered, but their COVs were in good consistency.
513 This is because all these equations use $e_1-d/2$ as the edge length of the shear plane, differing
514 only in terms of shear coefficient. All equations caused underestimations ranging from 4% to
515 49%, which were much worse than the prediction of the specimens with net section failures.

516 **5.5 End-splitting failure**

517 The ultimate load-carrying capacity of end-splitting failure is usually lower than that of shear
518 failure, which is important for 3D printed steel connections [45]. However, it is not stipulated
519 in many design standards, which is often judged to be a shear-out failure, as shown in Appendix
520 A.

521 In Equation (17), $e_1/e_2 = 0.5$ was used as the boundary of shear-out and end-splitting failure.
522 When $e_1/e_2 > 0.5$, it was considered that end-splitting failure would occur, and a simple uniform
523 reduction factor of 0.9 could be used based on the formula for shear-out failure [45]. It is worth
524 noting that the dimensions of all specimens met the condition of $e_1/e_2 > 0.5$, but only three

525 specimens presented end-splitting failure mode. This slightly affected the accuracy of Equation
526 (17), resulting in an underestimation of 20% and a COV of 0.10. However, when the reduction
527 factor was used for the three specimens, it resulted in the test-to-predicted ratio of 1.06, 1.09,
528 and 1.19 respectively, which needs further research to improve it.

529 **5.6 Tilt-bearing failure**

530 The tilt-bearing failure has not been incorporated into the current design standards. Appendix
531 A shows that different design standards calculated specimens with tilt-bearing failures as net
532 section tension or shear-out failures, resulting in underestimation or overestimation of the tilt-
533 bearing capacities.

534 Equation (18) was proposed to predict the capacities of the specimens failing in tilt-bearing. It
535 related the bearing capacity of tilt-bearing failure to plate dimensions, such as net length $b-d$,
536 bolt diameter d_b , and plate thickness t , which was consistent with the damage mechanism. It
537 showed satisfactory with an underestimation of 6% and a COV of 0.16.

538 **6. Conclusions**

539 In this paper, a total number of 24 coupon specimens with 3 different print layer orientations
540 and 36 single-shear connection specimens with 2 different print layer orientations and varying
541 dimensions were tested. The geometric properties of WAAM steel specimens were calculated
542 using a 3D laser scanner and a Matlab program. The measured material properties, geometries,
543 load-deformation characteristics, and failure modes were reported and analysed. The test
544 ultimate capacities were compared against the predictions of 6 available design standards and

545 other design approaches proposed in recent literature. According to the observation of the
546 experimental phenomenon and the analysis of the result data, the following conclusions can be
547 drawn:

548 1) In the WAAM coupon tests, except for Young's modulus, most of the other material
549 properties of specimens with a θ of 45° and 90° were consistently lower than those of
550 specimens with θ of 0° , with differences of up to 10%, which showed anisotropic material
551 properties of the WAAM steel plates. And the difference among the material properties of
552 specimens with θ of 45° and 90° was limited.

553 2) Four different failure modes, including net section, shear-out, end-splitting, and tilt-bearing
554 failure, were observed from the bolted connection tests. The print layer orientations ($\theta = 0^\circ$
555 and 90°) influenced the failure modes and load-carrying capacities of the WAAM
556 connections. Different failure modes were observed from 29% of the specimens with
557 similar dimensions but different print layer orientations. The difference in the ultimate
558 capacity of bolted connection specimens with θ of 0° and 90° reached up to 20%.

559 3) Current steel design standards cannot accurately predict the failure modes of WAAM steel
560 bolted connection specimens with the accuracy rates varying from 44% to 61%. This could
561 be attributed to the influence of anisotropic material properties of the WAAM steel plates
562 and the failure modes of tilt-bearing and the end-splitting not being considered in current
563 design provisions. The accurate predictions of the ultimate capacities of most design

564 approaches were obtained by a compromise of the incorrect failure modes of WAAM steel
565 bolted connection specimens.

566 4) The ultimate load-bearing capacities of WAAM steel bolted connection specimens could
567 be accurately predicted by the existing design standards, where AS/NZS 4600 [27]
568 performed the best with a test-to-predicted capacity ratio of 1.03 and a COV of 0.11. In
569 terms of different specific failure modes, the ultimate capacities of net section and shear-
570 out failure were precisely predicted by AISC 360 [30] and AS/NZS 4600 [27].

571 5) The equations proposed in recent literature for shear-out and tilt-bearing failure could well
572 predict the ultimate capacities with an underestimation of 4% and 6%, respectively. The
573 equation for end-splitting failure was not suitable for WAAM steel bolted connection
574 specimens. It is suggested that WAAM design methods for end-splitting failure should be
575 further researched in the future.

576 **Acknowledgement**

577 The authors would like to thank the financial supports from the National Natural Science
578 Foundation of China (NSFC) (Grant Number: 52208215), the Natural Science Foundation of
579 Zhejiang Province (Grant Number: LQ22E080008) and the Centre for Balance Architecture of
580 Zhejiang University. The author would also like to thank the code for WAAM geometry analysis
581 provided by the Steel Structures Group of Imperial College London. The help for the tests from
582 the technician Mr Xiaohua Ji from the Structures Lab is also appreciated.

Specimen	Test		AISI S100 (Eqs.1,3,7)		AISC 360 (Eqs.8-10)		EN 1993-1-3 (Eqs.12,13)		EN 1993-1-8 (Eqs.11,14)		AS/NZS 4600 (Eqs.1-3)		AS4100 (Eqs.4-6)		Eq.15	Eq.16	Eq.17	Eq.18
	FM	P_u (kN)	FM	$\frac{P_u}{P_{AISI}}$	FM	$\frac{P_u}{P_{AISC}}$	FM	$\frac{P_u}{P_{EN3}}$	FM	$\frac{P_u}{P_{EN8}}$	FM	$\frac{P_u}{P_{AS/NZS}}$	FM	$\frac{P_u}{P_{AS}}$	$\frac{P_u}{P_{TEH}}$	$\frac{P_u}{P_{XING}}$	$\frac{P_u}{P_{LYU}}$	$\frac{P_u}{P_{TEH}}$
HS-18-30-27	NS	23.44	NS	1.14	NS	1.09	NS	1.09	NS	1.09	NS	1.14	NS	1.28				
HS-18-40-27	NS	41.55	NS	1.09	NS	1.02	NS	1.02	NS	1.02	NS	1.09	NS	1.20				
HS-18-60-20	ES	32.70	SO	1.25	SO	1.00	SO	1.06	SO	1.10	SO	0.88	SO	1.50	0.93	0.86	1.06	
HS-18-70-22	SO	38.82	SO	1.45	SO	1.16	SO	1.20	SO	1.23	SO	1.00	SO	1.74	1.06	0.98	1.18	
HS-18-60-18	SO	32.10	SO	2.19	SO	1.75	SO	1.33	SO	1.37	SO	1.11	SO	2.63	1.30	1.16	1.32	
HS-18-60-22	SO	39.94	SO	1.41	SO	1.13	SO	1.20	SO	1.23	SO	1.00	SO	1.69	1.05	0.97	1.18	
HS-18-60-32	TB	52.99	SO	1.21	SO	0.97	SO	1.22	SO	1.27	SO	1.02	SO	1.45				1.07
HS-18-60-36	TB	48.36	SO	0.91	SO	0.73	SO	0.98	SO	1.01	SO	0.82	SO	1.10				1.00
HS-18-70-36	TB	74.97	SO	1.15	SO	0.92	SO	1.26	SO	1.31	SO	1.09	SO	1.39				1.27
HS-22-40-33	NS	31.75	NS	1.01	NS	0.96	NS	0.96	NS	0.96	NS	1.01	NS	1.13				
HS-22-50-33	NS	54.07	SO	1.15	NS	0.95	SO	1.08	SO	1.08	NS	1.01	SO	1.38				
HS-22-50-36	TB	47.68	NS	1.03	NS	0.97	NS	0.97	NS	0.97	NS	1.03	SO	1.16				0.94
HS-22-60-26	SO/ES	45.49	SO	1.30	SO	1.04	SO	1.13	SO	1.13	SO	0.94	SO	1.56	0.98	0.91	1.09	
HS-22-60-40	TB	58.96	SO	1.06	NS	0.88	SO	1.08	SO	1.09	NS	0.95	SO	1.27				1.07
HS-26-50-39	NS	40.08	NS	0.91	NS	0.86	NS	0.86	NS	0.86	NS	0.91	NS	1.02				
HS-26-70-47	TB	60.96	SO	0.88	NS	0.82	SO	0.92	SO	0.92	NS	0.88	SO	1.06				1.01

HS-26-60-29	SO	51.05	SO	1.77	SO	1.42	SO	1.35	SO	1.36	SO	1.12	SO	2.13	1.23	1.11	1.31	
HS-26-70-45	TB	68.19	SO	1.05	NS	0.92	SO	1.06	SO	1.08	NS	0.98	SO	1.26				1.11
VS-18-30-27	NS	21.81	NS	1.09	NS	1.04	NS	1.04	NS	1.04	NS	1.09	NS	1.23				
VS-18-40-27	NS	39.41	NS	1.11	NS	1.04	SO	1.05	NS	1.04	NS	1.11	SO	1.32				
VS-18-50-20	SO	34.98	SO	1.66	SO	1.33	SO	1.33	SO	1.22	SO	1.11	SO	2.00	1.19	1.09	1.30	
VS-18-70-22	SO	43.40	SO	1.64	SO	1.32	SO	1.43	SO	1.31	SO	1.19	SO	1.97	1.24	1.15	1.40	
VS-18-60-18	SO	33.40	SO	1.95	SO	1.56	SO	1.39	SO	1.30	SO	1.16	SO	2.34	1.29	1.17	1.39	
VS-18-60-22	SO	40.93	SO	1.74	SO	1.39	SO	1.44	SO	1.35	SO	1.20	SO	2.09	1.27	1.17	1.45	
VS-18-60-32	TB	50.80	SO	1.07	SO	0.86	SO	1.10	SO	1.02	SO	0.91	SO	1.29				0.93
VS-18-60-36	TB	49.64	SO	0.98	SO	0.78	SO	1.06	SO	0.98	SO	0.88	SO	1.18				1.08
VS-18-70-36	TB	59.37	SO	1.10	SO	0.88	SO	1.18	SO	1.11	SO	0.99	SO	1.32				1.13
VS-22-40-33	NS	33.31	NS	1.10	NS	1.04	NS	1.04	NS	1.04	NS	1.10	NS	1.23				
VS-22-50-33	NS	51.66	SO	1.26	NS	1.15	SO	1.21	NS	1.15	NS	1.22	SO	1.51				
VS-22-50-36	NS	45.76	NS	1.03	NS	0.96	SO	0.97	NS	0.96	NS	1.03	SO	1.17				
VS-22-60-26	SO	40.54	SO	1.50	SO	1.20	SO	1.21	SO	1.09	SO	1.01	SO	1.80	1.08	0.98	1.16	
VS-22-60-40	NS	62.59	SO	1.16	NS	0.99	SO	1.20	SO	1.08	NS	1.07	SO	1.39				
VS-26-50-39	TB	31.15	NS	0.73	NS	0.68	NS	0.68	NS	0.68	NS	0.73	NS	0.81				0.64
VS-26-70-47	TB	70.34	SO	1.12	NS	1.01	SO	1.15	SO	1.05	NS	1.08	SO	1.34				1.24
VS-26-60-29	ES	45.23	SO	1.61	SO	1.29	SO	1.21	SO	1.11	SO	1.01	SO	1.93	1.11	1.00	1.19	
VS-26-70-45	NS	73.61	SO	1.21	NS	1.05	SO	1.24	SO	1.12	NS	1.13	SO	1.46				1.29
FMPA			0.50		0.61		0.44		0.53		0.61		0.44					
Mean				1.25		1.06		1.13		1.10		1.03		1.48	1.14	1.04	1.25	1.06
COV				0.25		0.21		0.14		0.13		0.11		0.27	0.11	0.10	0.10	0.16

585 Note: FM = failure mode; NS: net section tension; SO: shear-out; ES: end-splitting; TB: tilt-bearing failure; FMPA: failure mode prediction accuracy and COV:
586 coefficient of variation.

587 **Reference**

- 588 [1] Buchanan C, Gardner L. Metal 3D printing in construction: a review of methods, research,
589 applications, opportunities and challenges. *Engineering Structures*. 2019;180:332-48.
- 590 [2] Duda T, Raghavan LV. 3D metal printing technology: the need to re-invent design practice.
591 *Ai & Society*. 2018;33:241-52.
- 592 [3] Ding D, Pan Z, Cuiuri D, Li H. Wire-feed additive manufacturing of metal components:
593 technologies, developments and future interests. *The International Journal of Advanced*
594 *Manufacturing Technology*. 2015;81:465-81.
- 595 [4] Wu B, Pan Z, Ding D, Cuiuri D, Li H, Xu J et al. A review of the wire arc additive
596 manufacturing of metals: properties, defects and quality improvement. *Journal of*
597 *Manufacturing Processes*. 2018;35:127-39.
- 598 [5] Gardner L, Kyvelou P, Herbert G, Buchanan C. Testing and initial verification of the world's
599 first metal 3D printed bridge. *Journal of Constructional Steel Research*. 2020;172:106233.
- 600 [6] Feucht T, Waldschmitt B, Lange J, Erven M. Additive manufacturing of a bridge in situ.
601 *Steel Construction*. 2022;15:100-10.
- 602 [7] Zuo W, Chen M, Chen Y, Zhao O, Cheng B, Zhao J. Additive manufacturing oriented
603 parametric topology optimization design and numerical analysis of steel joints in gridshell
604 structures. *Thin-Walled Structures*. 2023;188:110817.
- 605 [8] Ye J, Kyvelou P, Gilardi F, Lu H, Gilbert M, Gardner L. An end-to-end framework for the
606 additive manufacture of optimized tubular structures. *IEEE Access*. 2021;9:165476-89.
- 607 [9] Ermakova A, Mehmanparast A, Ganguly S, Razavi N, Berto F. Investigation of mechanical
608 and fracture properties of wire and arc additively manufactured low carbon steel components.
609 *Theoretical and Applied Fracture Mechanics*. 2020;109:102685.
- 610 [10] Huang C, Kyvelou P, Zhang R, Ben Britton T, Gardner L. Mechanical testing and
611 microstructural analysis of wire arc additively manufactured steels. *Materials & Design*.
612 2022;216:110544.
- 613 [11] Kyvelou P, Slack H, Buchanan C, Wade MA, Gardner L. Material testing and analysis of
614 WAAM stainless steel. 2021;4:1702-9.
- 615 [12] Kyvelou P, Slack H, Daskalaki Moutanou D, Wade MA, Britton TB, Buchanan C et al.
616 Mechanical and microstructural testing of wire and arc additively manufactured sheet material.
617 *Materials & Design*. 2020;192:108675.
- 618 [13] Lin Z, Goulas C, Ya W, Hermans MJM. Microstructure and mechanical properties of
619 medium carbon steel deposits obtained via wire and arc additive manufacturing using metal-
620 cored wire. *Metals*. 2019;9:673.

- 621 [14] Sun L, Jiang F, Huang R, Yuan D, Guo C, Wang J. Anisotropic mechanical properties and
622 deformation behavior of low-carbon high-strength steel component fabricated by wire and arc
623 additive manufacturing. *Materials Science and Engineering: A*. 2020;787:139514.
- 624 [15] Guo C, Liu M, Hu R, Yang T, Wei B, Chen F et al. High-strength wire + arc additive
625 manufactured steel. *International Journal of Materials Research*. 2020;111:325-31.
- 626 [16] Hadjipantelis N, Weber B, Buchanan C, Gardner L. Description of anisotropic material
627 response of wire and arc additively manufactured thin-walled stainless steel elements. *Thin-
628 Walled Structures*. 2022;171:108634.
- 629 [17] Buchanan C, Real E, Gardner L. Testing, simulation and design of cold-formed stainless
630 steel CHS columns. *Thin-Walled Structures*. 2018;130:297-312.
- 631 [18] Laghi V, Palermo M, Gasparini G, Girelli VA, Trombetti T. Experimental results for
632 structural design of wire-and-arc additive manufactured stainless steel members. *Journal of
633 Constructional Steel Research*. 2020;167:105858.
- 634 [19] Kyvelou P, Huang C, Gardner L, Buchanan C. Structural testing and design of wire arc
635 additively manufactured square hollow sections. *Journal of Structural Engineering*.
636 2021;147:04021218.
- 637 [20] Huang C, Meng X, Buchanan C, Gardner L. Flexural buckling of wire arc additively
638 manufactured tubular columns. *Journal of Structural Engineering*. 2022;148:04022139.
- 639 [21] Huang C, Meng X, Gardner L. Cross-sectional behaviour of wire arc additively
640 manufactured tubular beams. *Engineering Structures*. 2022;272:114922.
- 641 [22] Guo X, Kyvelou P, Ye J, Gardner L. Experimental investigation of wire arc additively
642 manufactured steel T-stub connections. *Journal of Constructional Steel Research*.
643 2023;211:108106.
- 644 [23] Ye J, Quan G, Yun X, Guo X, Chen J. An improved and robust finite element model for
645 simulation of thin-walled steel bolted connections. *Engineering Structures*. 2022;250:113368.
- 646 [24] Ye J, Quan G, Kyvelou P, Teh L, Gardner L. A practical numerical model for thin-walled
647 steel connections and built-up members. *Structures*. 2022;38:753-64.
- 648 [25] Quan G, Ye J, Li W. Computational modelling of cold-formed steel lap joints with screw
649 fasteners. *Structures*. 2021;33:230-45.
- 650 [26] Winter G. Tests on bolted connections in light gage steel. *Journal of the Structural Division*.
651 1956;82:920-1.
- 652 [27] AS/NZS 4600. Cold-formed steel structures. Sydney: Australian/New Zealand Standard;
653 2018.
- 654 [28] AS 4100. Steel structures. Australia: Standards Association of Australia; 2020.
- 655 [29] AISI S100. North American specification for the design of cold-formed steel structural

656 members. Washington DC: American Iron and Steel Institute; 2016.

657 [30] AISC 360. Specification for structural steel buildings. Chicago: American Institute of Steel
658 Construction; 2022.

659 [31] Eurocode 3: design of steel structures – part 1-1: general rules and rules for building.
660 Brussels: European Committee for Standardisation; 2020.

661 [32] Eurocode 3 - design of steel structures - part 1-3: general rules - supplementary rules for
662 cold-formed members and sheeting. Brussels: European Committee for Standardisation; 2022.

663 [33] Eurocode 3: design of steel structures – part 1-8: design of joints. Brussels: European
664 Committee for Standardisation; 2021.

665 [34] Bhuiyan RA, Ahmed A, Teh LH. Ultimate bearing capacity of unconfined bolted
666 connections in cold-formed steel members. Journal of Structural Engineering.
667 2021;147:04021048.

668 [35] Xing H, Teh LH, Jiang Z, Ahmed A. Shear-out capacity of bolted connections in cold-
669 reduced steel sheets. Journal of Structural Engineering. 2020;146:04020018.

670 [36] Clements DDA, Teh LH. Active shear planes of bolted connections failing in block shear.
671 Journal of Structural Engineering. 2013;139:320-7.

672 [37] Teh LH, Uz ME. Ultimate shear-out capacities of structural-steel bolted connections.
673 Journal of Structural Engineering. 2015;141:04014152.

674 [38] Teh LH, Gilbert BP. Net section tension capacity of bolted connections in cold-reduced
675 steel sheets. Journal of Structural Engineering. 2012;138:337-44.

676 [39] Salih EL, Gardner L, Nethercot DA. Numerical investigation of net section failure in
677 stainless steel bolted connections. Journal of Constructional Steel Research. 2010;66:1455-66.

678 [40] Salih EL, Gardner L, Nethercot DA. Bearing failure in stainless steel bolted connections.
679 Engineering Structures. 2011;33:549-62.

680 [41] Kim TS, Kuwamura H, Kim S, Lee Y, Cho T. Investigation on ultimate strength of thin-
681 walled steel single shear bolted connections with two bolts using finite element analysis. Thin-
682 Walled Structures. 2009;47:1191-202.

683 [42] Soo Kim T, Kuwamura H. Finite element modeling of bolted connections in thin-walled
684 stainless steel plates under static shear. Thin-Walled Structures. 2007;45:407-21.

685 [43] Kim TS, Kuwamura H, Cho TJ. A parametric study on ultimate strength of single shear
686 bolted connections with curling. Thin-Walled Structures. 2008;46:38-53.

687 [44] Wang YB, Lyu YF, Li GQ, Liew JYR. Behavior of single bolt bearing on high strength
688 steel plate. Journal of Constructional Steel Research. 2017;137:19-30.

689 [45] Lyu YF, Wang YB, Li GQ, Jiang J. Numerical analysis on the ultimate bearing resistance

690 of single-bolt connection with high strength steels. *Journal of Constructional Steel Research*.
691 2019;153:118-29.

692 [46] Teh Lip H, Uz Mehmet E. Ultimate tilt-bearing capacity of bolted connections in cold-
693 reduced steel sheets. *Journal of Structural Engineering*. 2017;143:04016206.

694 [47] Ding C, Torabian S, Schafer BW. Strength of bolted lap joints in steel sheets with small
695 end distance. *Journal of Structural Engineering*. 2020;146:04020270.

696 [48] Guo X, Kyvelou P, Ye J, Teh LH, Gardner L. Experimental investigation of wire arc
697 additively manufactured steel single-lap shear bolted connections. *Thin-Walled Structures*.
698 2022;181:110029.

699 [49] Tonelli L, Laghi V, Palermo M, Trombetti T, Ceschini L. AA5083 (Al–Mg) plates produced
700 by wire-and-arc additive manufacturing: effect of specimen orientation on microstructure and
701 tensile properties. *Progress in Additive Manufacturing*. 2021;6:479-94.

702 [50] Hu Q, Miao J, Wang X, Li C, Fang K. Microstructure and properties of ER50-6 steel
703 fabricated by wire arc additive manufacturing. *Scanning*. 2021;2021:7846116.

704 [51] Ding DH, Pan ZX, Dominic C, Li HJ. Process planning strategy for wire and arc additive
705 manufacturing. *Robotic Welding, Intelligence and Automation*. 2015:437-50.

706 [52] Chen M, Young B. Tensile tests of cold-formed stainless steel tubes. *Journal of Structural*
707 *Engineering*. 2020;146:04020165.

708 [53] Chen M, Zhang T, Young B. Behavior of concrete-filled cold-formed steel built-up section
709 stub columns. *Thin-Walled Structures*. 2023;187:110692.

710 [54] Chen M, Cai A, Pandey M, Shen C, Zhang Y, Hu L. Mechanical properties of high strength
711 steels and weld metals at arctic low temperatures. *Thin-Walled Structures*. 2023;185:110543.

712 [55] Rogers CA, Hancock GJ. Failure modes of bolted-sheet-steel connections loaded in shear.
713 *Journal of Structural Engineering*. 2000;126:288-96.

714 [56] Huang Y, Young B. The art of coupon tests. *Journal of Constructional Steel Research*.
715 2014;96:159-75.

716 [57] Pan B. Digital image correlation for surface deformation measurement: historical
717 developments, recent advances and future goals. *Measurement Science and Technology*.
718 2018;29:082001.

719 [58] Jiang B, Yam MCH, Ke K, Lam ACC, Zhao Q. Block shear failure of S275 and S690 steel
720 angles with single-line bolted connections. *Journal of Constructional Steel Research*.
721 2020;170:106068.

722

723